Physics of the Earth and Planetary Interiors 229 (2014) 110–121

Contents lists available at ScienceDirect

Physics of the Earth and Planetary Interiors

journal homepage: www.elsevier.com/locate/pepi

Can downwelling at the top of the Earth's core be detected in the geomagnetic secular variation?

Hagay Amit

CNRS, Université de Nantes, Nantes Atlantiques Universités, UMR CNRS 6112, Laboratoire de Planétologie et de Géodynamique, 2 rue de la Houssinière, F-44000 Nantes, France

ARTICLE INFO

Article history:
Received 22 May 2013
Received in revised form 7 January 2014
Accepted 16 January 2014
Available online 24 January 2014
Edited by C. Jones

Keywords:
Geomagnetic secular variation
Downwelling
Core flow
Core–mantle boundary
Stable stratification

ABSTRACT

It has been argued based on recent seismic and mineral physics studies that the top of Earth's liquid outer core is stably stratified. Here I analyze persistent geomagnetic secular variation features on the core–mantle boundary to examine whether a kinematic signature of core fluid upwelling/downwelling can be detected. I focus on regions of intense high-latitude geomagnetic flux patches that may be maintained by fluid downwelling. In order to identify persistent patterns, the radial field and its secular variation are stacked in the flux patch moving reference frame. These stacked images are compared with forward solutions to the radial induction equation based on idealized field-flow models. Clear advective secular variation signature below North America indicates that these intense flux patches may exhibit significant mobility. Stretching signature in the form of persistent positive secular variation correlated with the intense flux patch below the Southern Indian Ocean may be considered as regional scale geomagnetic evidence for whole core convection, although pure toroidal flow cannot be outruled.

1. Introduction

The geomagnetic field is generated by dynamo action driven by convection in Earth's liquid metallic outer core. The style of convection is in general thermochemical - secular cooling drives thermal convection, whereas light element release by the freezing inner core drives compositional convection (e.g. Olson, 2007). Uncertainties in the precise adiabatic temperature profile in the outer core and in the magnitude of the heat flux across the core–mantle boundary (CMB) pose uncertainty on whether the present day convection in the outer core has any significant thermal contribution, in particular at the top of the core (e.g. Lay et al., 2008). Recent seismic studies (Helffrich and Kaneshima, 2010) and new estimates of large core thermal and electrical conductivities from mineral physics calculations (Pozzo et al., 2012; Vlcek et al., 2012) indeed suggest that the top of the core is stably stratified (Gubbins and Davies, 2013).

Can time-dependent geomagnetic field models help elucidate whether upwelling/downwelling prevail at the top of the core? Two approaches have been employed so far to address this question. On global scale, core flow inversions may be used to reveal whether poloidal flow is required to explain the observed geomagnetic secular variation (SV). Pure toroidal core flow models consistent with stable stratification at the top of the core (Gubbins, 1982; Bloxham, 1989, 1992; Holme and Olsen, 2006; Olsen and Mandea, 2008) showed that it is possible to fit (to a certain level) the observed SV without magnetic field stretching. However, because of the severe non-uniqueness associated with core flow inversions (Bloxham and Jackson, 1991; Holme, 2007), explaining the SV with pure toroidal flow cannot be considered as a proof for the non-existence of upwelling. For example, Rau et al. (2000) have demonstrated using synthetic data from numerical dynamos that both pure toroidal and tangential geostrophic flows may explain the SV. Even if upwelling is permitted, most core flow models are dominantly toroidal (see Finlay and Amit, 2011, and references therein). Nevertheless, Whaler, 1986 argued that a poloidal flow contribution is needed to adequately explain the SV, and moreover, it is even possible to recover the observed SV with a pure poloidal flow (Beggan and Whaler, 2008). Overall, the observed SV may constrain the dominant toroidal core flow component, while the coupling between toroidal and poloidal flows, and hence the upwelling existence and pattern, largely depend on the apriori physical assumption that is incorporated in the inversions.

Another approach to examine the existence of upwelling just below the CMB is pointwise, i.e. to evaluate the geomagnetic SV at radial field extreme points. At these special points the radial field horizontal gradient is zero, so no SV is generated by advection. Under the frozen-flux approximation (Roberts and Scott, 1965), the only remaining effect that may produce SV at these points is magnetic field stretching by upwelling. Whaler (1980) argued that

E-mail address: Hagay.Amit@univ-nantes.fr

http://dx.doi.org/10.1016/j.pepi.2014.01.012
0031-9201/

relatively weak SV at extreme points suggests no upwelling and stable stratification at the top of the core. However, uncertainties in the precise locations of these extreme points render such an analysis unreliable (Whaler and Holme, 2007).

Here I propose to analyze geomagnetic SV on a regional scale rather than global (core flow inversions) or pointwise (extreme radial field points). In particular, I focus on regions of intense geomagnetic flux patches. These robust features are present in geomagnetic field models spanning various timescales (Kelly and Gubbins, 1997; Jackson et al., 2000; Korte et al., 2009). Numerical dynamos reproduce well the observed high-latitude intense flux patches (e.g. Christensen et al., 2010). In these simulations the origin of intense flux patches on the outer boundary is fluid downwelling at the top of the core that concentrates field lines (Christensen et al., 1998; Olson and Christensen, 2002; Amit et al., 2010). The time-average locations of these correlated fluid downwelling and magnetic flux patches are prescribed by lower mantle thermal heterogeneity (e.g. Gubbins, 2003) although on a snapshot the patches may be found elsewhere (Bloxham, 2002; Amit et al., 2010). Directly related to a thermal mantle anomaly or not, the kinematic relation between concentrated flux and fluid downwelling is expected from the stretching term in the radial magnetic induction equation.

In this paper I search for a downwelling signature in the SV at regions of intense geomagnetic flux patches. I stack SV images in the patch moving reference frame to reveal the persistent nature of the regional field variation. Stacked SV patterns are interpreted by comparison with some idealized SV patterns produced by forward solutions to the radial induction equation. These forward solutions rely on idealized field and flow models, which are based on some simple inferences from geomagnetic observations, rotating flows theory and numerical dynamo simulations.

Previous analyses of regional geomagnetic SV focused on the north polar region. Olson and Aurnou (1999) inverted the time-average radial geomagnetic field and SV at this region for the axisymmetric steady core flow. They found a persistent westward (anticyclonic) polar vortex and fluid upwelling inside the northern hemisphere tangent cylinder. Chulliat et al. (2010) observed a bipolar SV structure centered at an emerging reversed flux patch at the north polar region, which they interpreted as the signature of upwelling and magnetic flux expulsion by radial diffusion.

As mentioned above, in this study radial field and SV images are stacked to obtain time-averages in a patch moving reference frame. Stacking is common practice in seismology. Seismograms of many earthquakes are ordered in distance and plotted vs. travel-time to reduce random noise, resulting in coherent travel-time branches which represent different seismic waves traveling through the Earth's interior (e.g. Shearer, 1991; Lay and Wallace, 1995). In paleomagnetism, stacking was recently applied to find dynamic similarity of polarity reversals. By stacking the ten most detailed volcanic records and assuming same reversal duration, Valet et al. (2012) found that the reversal process includes three steps, a precursory event, the polarity transition and the rebound, each step characterized by the same time constant.

The paper is outlined as follows. In Section 2 the stacking and forward solution methods are described. The idealized field and flow models that are used to obtain forward solutions of the radial induction equation at the top of the core are introduced. In Section 3 the results of the stacked geomagnetic field and SV images are presented and compared with the idealized SV from the forward solutions. A snapshot from a recent geomagnetic field model derived from satellite and surface observatories data is also considered. In Section 4 the results are discussed, in particular their implications for the possibility of stable stratification at the top of the core.

2. Method

2.1. Stacking at regions of intense flux patches

I use the historical geomagnetic field model *gufm1* of Jackson et al. (2000) for the period 1840–1990. The centers of intense high-latitudes flux patches are taken from the timeseries obtained by Amit et al. (2011). The two northern hemisphere patches are classified as intense throughout the entire period 1840–1990, whereas in the southern hemisphere in some years only one patch is classified as intense.

At each snapshot, around a center of patch a fixed longitudinal and latitudinal range is considered. Next, a rotational transformation about the center of a patch is performed based on its orientation with respect to the center of the same patch in the previous snapshot. The pole of the initial snapshot is arbitrarily set to the north geographic pole. The rotational angle at time t_i is then defined by the angle between the centers of patches at times t_i and t_{i-1} and the westward direction. Defined this way, if a patch is only drifting without changing its shape (but in time-dependent directions), the stacked SV will show a bipolar pair oriented in the east–west direction. Any deviation from such pattern indicates the action of other kinematic processes. For more details on the rotational transformation see the Appendix.

To illustrate the importance of applying a rotational transformation, in particular for obtaining meaningful stacked SV patterns, consider a patch drifting and completing a full circle. The SV pattern at each snapshot will exhibit a bipolar structure. However, if only a translational transformation is performed, the bipolar SV will change its orientation with time encompassing all angles of

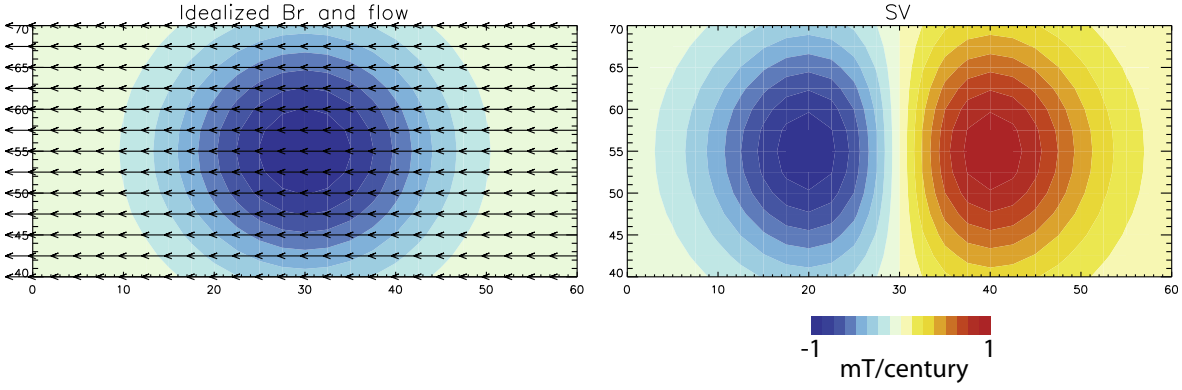

Fig. 1. Idealized translation. Left: Vertical field (colors) and horizontal flow (arrows); Right: SV. (For interpretation of the references to colour in this figure legend, the reader is referred to the web version of this article.)

Table 1
Parameters of the idealized SV models (see definitions in text).

Case	Kinematics	k	$\delta\phi$	λ^*
1	Advection	0.1	20°	0
2	Stretching	0.1	0°	0
3	Advection/stretching	0.5	10°	0
4	Diffusion	0.5	10°	100

the circle and the stacked SV will amount to zero. The rotational transformation follows the instantaneous orientation of the patch and would therefore maintain a bipolar SV pattern consistent with a drifting stationary patch.

Once both translational and rotational transformations were applied, the radial field and its SV around each patch are stacked. For each patch, the stacking is performed over the period in which it was classified as intense by Amit et al. (2011).

2.2. Idealized field and flow models at regions of intense flux patches

The idealized radial field of an intense magnetic flux patch is modeled as a 2D isotropic Gaussian. For simplicity, a local Cartesian coordinate system is used. The radial field B_r is then given by

$$B_r = B_0 \cdot e^{-\frac{h_b^2}{2\sigma^2}} \tag{1}$$

where B_0 is the amplitude, h_b is the distance from the center of the magnetic flux patch and σ is the standard deviation which represents the width of the patch. The field amplitude is set to $B_0 = 1$ mT, and the standard deviation is arbitrarily set to $\sigma = 10^\circ$.

The total SV is comprised of a simple patch drift due to advection by a uniform jet plus induction effects due to the interaction between a more complex flow and the field. Fig. 1 presents the translational SV produced by a uniform westward flow advecting the idealized radial field model. The SV is characterized by a

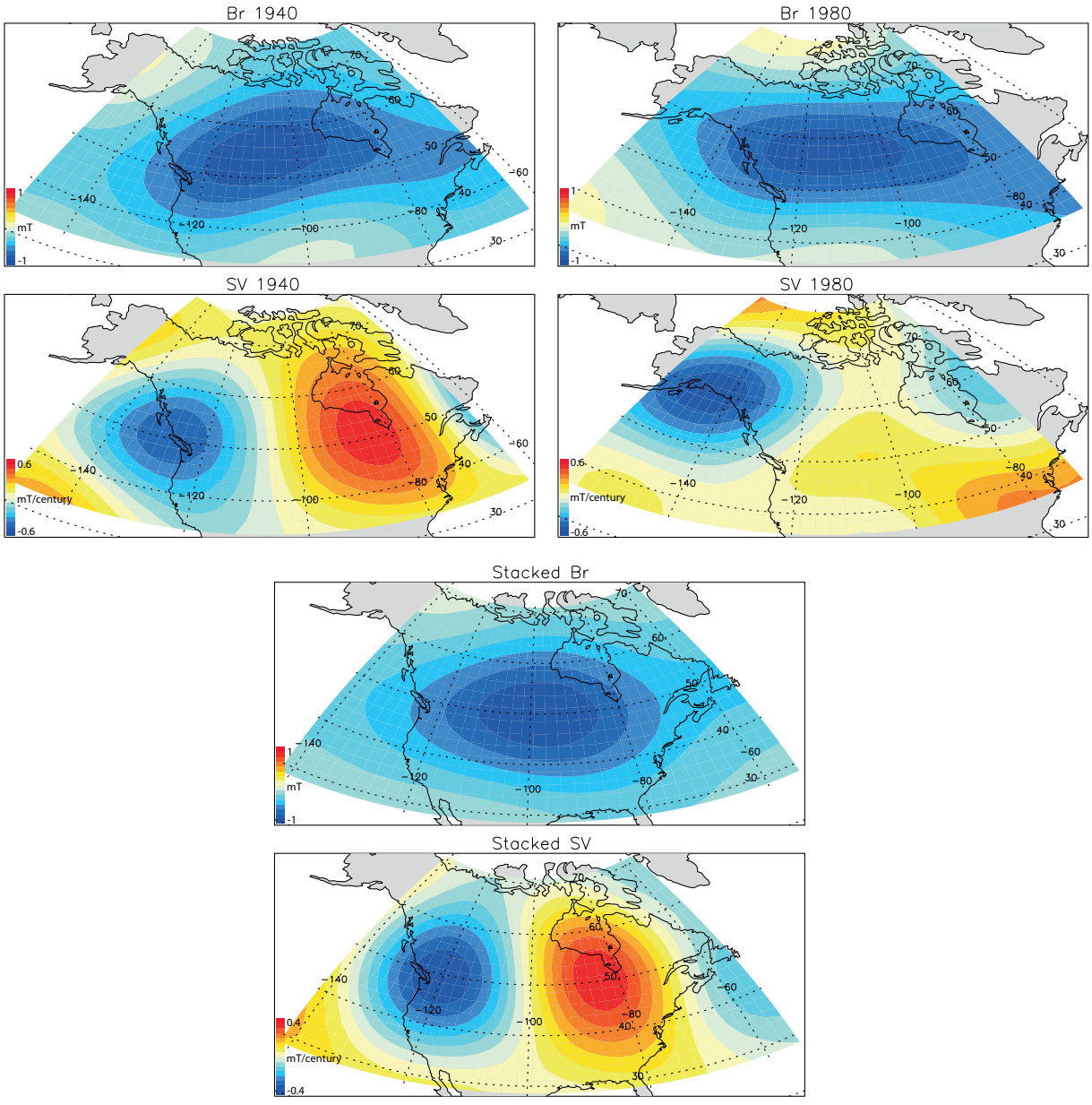

Fig. 2. Radial field and SV centered below the North America geomagnetic flux patch at 1940 (top left), 1980 (top right) and stacked over the period 1840–1990 (bottom). The images are based on the historical field model *gufm1* of Jackson et al. (2000). The stacking is performed based on the time-dependent centers of patches identified by Amit et al. (2011).

bipolar structure with zero coincident with the center of the patch.

Next, the idealized toroidal flow around an intense magnetic flux patch is modeled as a classical circular Rankine vortex patch (Rankine, 1858), which is often used as a simple description of large-scale atmospheric systems (e.g. Ghil and Solan, 1973; Ide and Ghil, 1997; Brown et al., 2005; Harvey and Ambaum, 2011). The toroidal flow potential $\mathcal{T}$ is given by

$$\mathcal{T} = \begin{cases} -\frac{1}{4}\zeta\left(h^2 - H^2\right) & \text{if } h < H \\ -\frac{1}{2}\zeta H^2 ln\left(\frac{h}{H}\right) & \text{if } h > H \end{cases} \tag{2}$$

where h is the distance from the center of the vortex and ζ is the (constant) perpendicular vorticity in the inner region ($h < H$). The corresponding azimuthal velocity in local polar coordinates is

$$u_t = -\frac{\partial \mathcal{T}}{\partial h} = \begin{cases} \frac{1}{2}\zeta h & \text{if } h < H \\ \frac{1}{2}\zeta \frac{H^2}{h} & \text{if } h > H \end{cases} \tag{3}$$

At the inner part of the vortex ($h < H$) the flow obeys solid body rotation and the vorticity perpendicular to the plane of motion is constant, whereas at the outer part ($h > H$) the flow decreases with distance and the vorticity vanishes. The vorticity is set to give a maximal toroidal flow of 10 km/yr, and the extent of the inner part of the vortex is set to $H = 5^\circ$.

Next, the poloidal flow is coupled to the toroidal flow via a helical flow relation:

$$\nabla_h \cdot \vec{u}_h = \mp k\zeta \tag{4}$$

where $\vec{u}_h$ is the horizontal velocity vector, the $\mp$ sign applies to the northern/southern hemisphere respectively and k represents the relative strength of the poloidal flow for a given toroidal flow. The helical flow relation was observed in numerical dynamos (Olson et al., 2002; Amit et al., 2007) and in some analytical examples of rotating convecting systems (Amit and Olson, 2004). I arbitrarily consider here the northern hemisphere, so B_0 is negative in (1) and the negative sign applies in (4).

The vortex is separated from the magnetic flux patch by a lateral distance $\delta\phi$. In numerical dynamo models, intense flux patches are characterized by a large amount of field-aligned flow (Amit et al., 2010; Finlay and Amit, 2011), so $\delta\phi$ is small. In reality, due to the large disparity between the viscous and magnetic diffusion times in the core (as opposed to their comparable values in the dynamo models), the vortex and flux patch may be shifted from each other. For generality, $\delta\phi$ is considered here as a free parameter.

The idealized field and flow models are used to calculate the SV from the radial magnetic induction equation at the top of the core:

$$\frac{\partial B_r}{\partial t} + \vec{u}_h \cdot \nabla B_r + B_r \nabla_h \cdot \vec{u}_h = \lambda\left(\frac{\partial^2 B_r}{\partial r^2} + \nabla_h^2 B_r\right) \tag{5}$$

where r is the vertical coordinate. The first term in (5) is the SV, the second is the advective contribution by both toroidal and poloidal flows, the third is the stretching contribution and the last term represents magnetic diffusion. Recall that (5) is considered in a local Cartesian coordinates system. According to the frozen-flux approximation, both magnetic diffusion terms on the right hand side of (5) are often assumed negligible (Roberts and Scott, 1965). Knowledge of the radial field on the CMB allows calculating the horizontal diffusion, but radial derivatives are unknown so radial diffusion cannot be inferred from field models. Numerical dynamo models show a correlation between horizontal and radial diffusion (Amit and Christensen, 2008). They therefore rewrote (5) as

$$\frac{\partial B_r}{\partial t} + \vec{u}_h \cdot \nabla B_r + B_r \nabla_h \cdot \vec{u}_h \simeq \lambda^* \nabla_h^2 B_r \tag{6}$$

where λ^* is an effective magnetic diffusivity which accounts for the small length scale associated with radial diffusion. Based on an extrapolation of a scaling law derived from their dynamo models, Amit and Christensen (2008) estimated $\lambda^* = 100 - 1000$ for Earth's core, in agreement with estimates based on reversed flux intensification in geomagnetic field models (Chulliat and Olsen, 2010). Here I assume in three cases frozen-flux, i.e. $\lambda^* = 0$, and in another case magnetic diffusion is accounted for with $\lambda^* = 100$.

Different choices of the parameters characterizing the lateral extent of the idealized flux patch and vortex, σ and H respectively, affect the overlap between the field and the flow structures and subsequently the resulting SV. Smaller values of σ and H reduce the overlap and the SV; However, smaller distance between the field and flow structures $\delta\phi$ recovers a stronger SV. The parameter

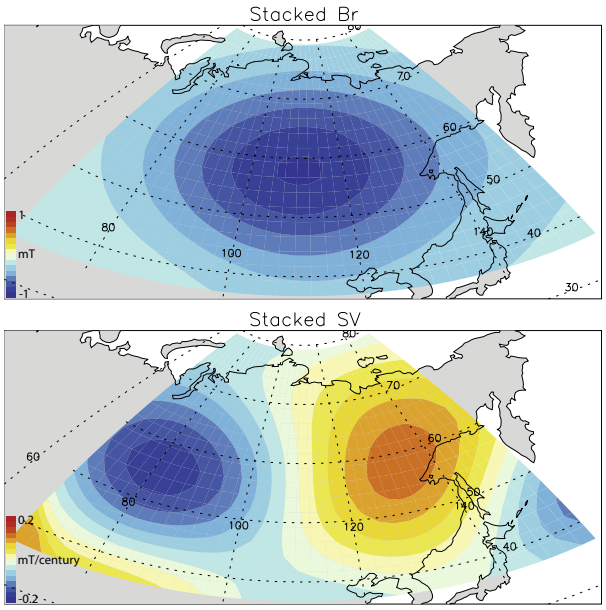

Fig. 3. As in Fig. 2 for the stacked Siberia geomagnetic flux patch. The stacking period is 1840–1990.

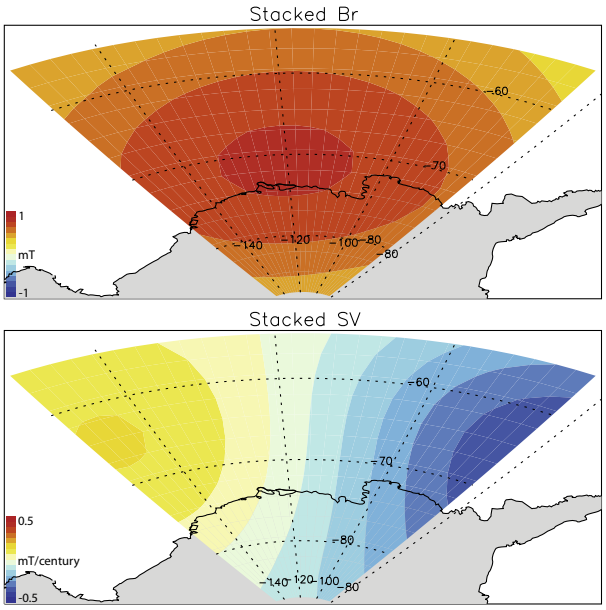

Fig. 4. As in Fig. 2 for the stacked Southern Pacific Ocean geomagnetic flux patch. The stacking period is 1840–1985.

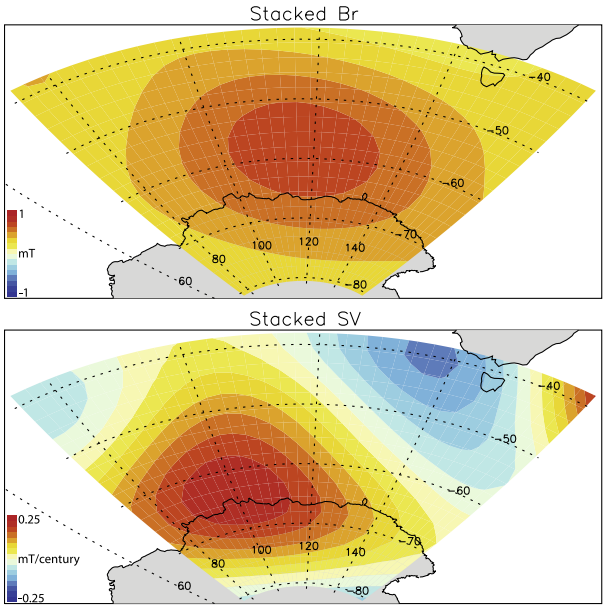

Fig. 5. As in Fig. 2 for the stacked Southern Indian Ocean geomagnetic flux patch. The stacking period is 1920–1990.

ζ characterizing the vortex magnitude affects the SV magnitude, but not its pattern.

In summary, the idealized SV models depend on three free parameters: the separation distance between the magnetic flux patch and the vortex $\delta\phi$, the relative strength of the poloidal flow k, and the effective magnetic diffusivity λ^*. Different combinations of these parameters yield different kinematic scenarios. Table 1 summarizes the free parameters of four idealized models that demonstrate the expected signature of SV due to advection, stretching, combined advection/stretching and diffusion, respectively.

3. Results

3.1. Stacked geomagnetic field and secular variation models

Fig. 2 shows two snapshots of the intense geomagnetic flux patch below North America with their respective SV maps (top) as well as the stacked images for the period 1840–1990 (bottom). All maps are centered at the center of the patch, and these patch-centered coordinates are used to calculate the stacked field and SV. Of the four high-latitude flux patches observed during the historical era, the North America patch is the most mobile. Based on the identification and tracking algorithm of Amit et al. (2011), between 1840 and 1990 this patch has moved $\sim 33.2^\circ$ westward and $\sim 14.5^\circ$ northward, or an azimuthal angular velocity of $\sim 0.22^\circ$/yr, comparable (in terms of angular velocity) to that of equatorial westward drifting patches (e.g. Hulot et al., 2002) that are considered the fastest over the CMB.

The radial field snapshots show similar morphology, but the SV snapshots exhibit somewhat different patterns. This time dependence motivates the examination of some kind of time-average.

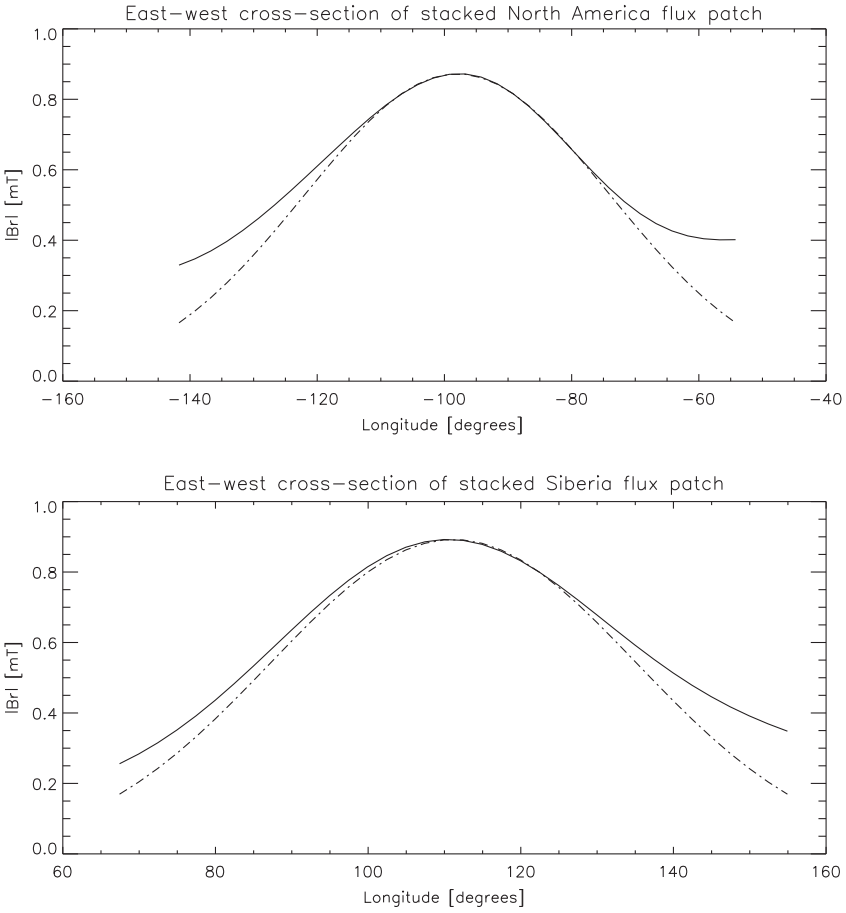

Fig. 6. East–west cross-sections of the stacked radial fields below North America (top) and Siberia (bottom). Solid lines denote the stacked radial field and dashed lines the Gaussian fits. The same Gaussian width was used for both fits.

Stacking in the patch moving reference frame is the most appropriate because it follows precisely the SV associated with the moving flux patch. The stacked SV below North America shows a clear bipolar structure with zero correlated with the center of the flux patch and negative upwind to the west, which was defined as the reference drift direction for the rotational transformation. This stacked SV pattern is therefore consistent with a simple drift of the North America patch (compare with Fig. 1).

Fig. 3 shows the stacked radial field and its SV for the Siberia patch. The magnitude of the stacked SV below Siberia is weaker than that of North America (note different scales between Fig. 2 bottom and Fig. 3). However, the pattern of symmetric bipolar SV characterizes the Siberia stacked patch as well, so it is also suggestive of a simple drift (Fig. 1). The stacked SV below the Southern Pacific Ocean patch (Fig. 4) shows a bipolar structure, but it is centered west to the center of the radial field structure, and in addition it is clearly asymmetric. The SV associated with this patch is characterized by stronger magnitude than those of the other three patches (again compare scales). Finally, In contrast to the other three patches, the stacked radial field and its SV below the Southern Indian Ocean patch (Fig. 5) shows an overall intensification, with positive SV covering most of the Southern Indian Ocean flux patch.

The stacked images allow testing the Gaussian approximation for the idealized radial field model. Fig. 6 shows east–west cross-sections of the stacked radial fields below North America and Siberia (solid lines) with the corresponding Gaussian fits (dashed lines). The cross-sections are symmetric about their centers, permitting decent fits. The Gaussian fits are especially good around the peak of field intensity where important SV is expected. Far from the centers of the flux patches the fitted curves fall somewhat more rapidly than the stacked geomagnetic field, but very far from the center of the patch the generated SV is expected to be weaker. Similar cross-sections with comparably good Gaussian fits were obtained for the other two stacked patches. Based on these fits, the idealized Gaussian radial field model for a localized intense magnetic flux patch seems a reasonable zeroth order approximation.

3.2. Forward secular variation from idealized field and flow models

Next the idealized field and flow models are applied to forward calculate the SV at a region of magnetic flux patch. Four cases are considered, each representing a different kinematic scenario (Table 1). In the first three cases magnetic diffusion is neglected. In case 1 the poloidal flow is set to be relatively weak (low k) and

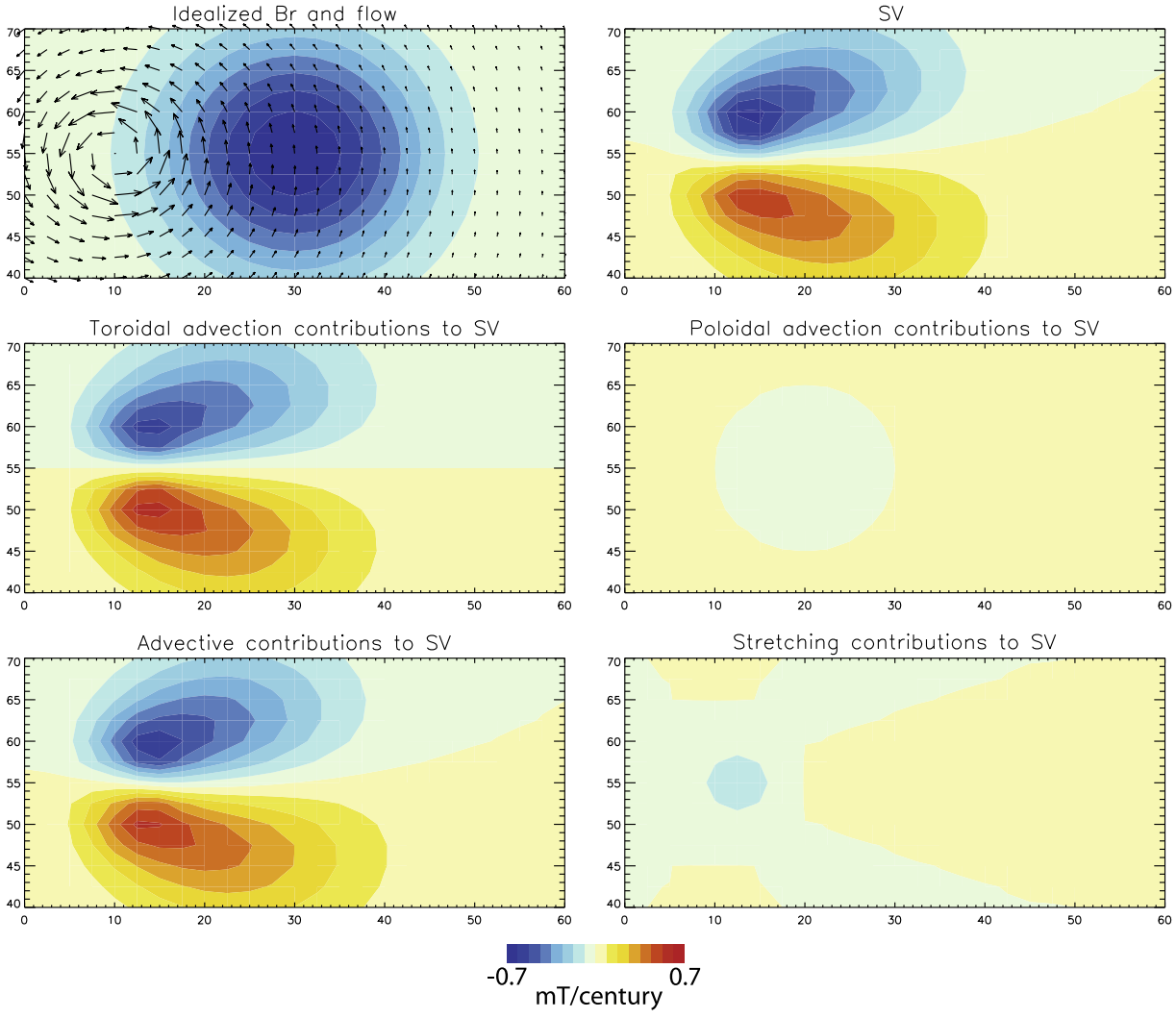

Fig. 7. Idealized case 1: Advection. Top left: Vertical field (colors) and horizontal flow (arrows); Top right: Total SV; Middle left: Toroidal advective contributions to SV; Middle right: Poloidal advective contributions to SV; Bottom left: Total advective contributions to SV; Bottom right: Stretching contributions to SV. The color bar corresponds to the SV subplots; The same color bar applies to the radial field with a range of ±1 mT. (For interpretation of the references to colour in this figure legend, the reader is referred to the web version of this article.)

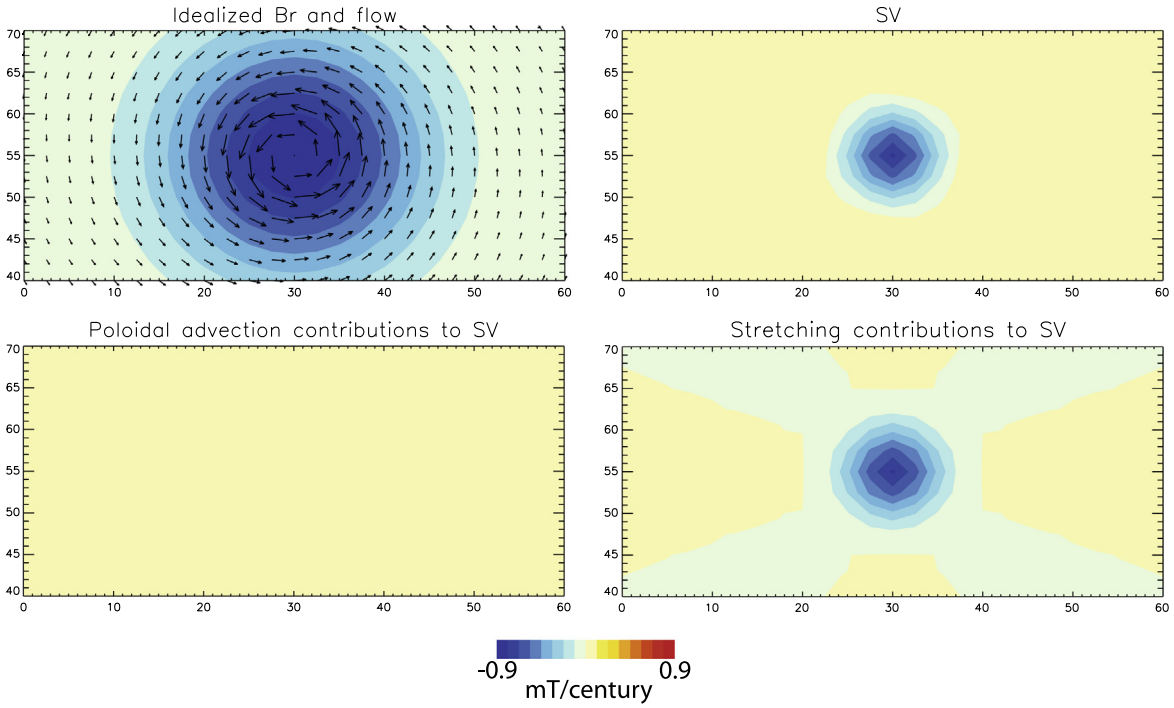

Fig. 8. Idealized case 2: Stretching. Top left: Vertical field (colors) and horizontal flow (arrows); Top right: Total SV; Middle left: Poloidal advective contributions to SV; Middle right: Stretching contributions to SV. (For interpretation of the references to colour in this figure legend, the reader is referred to the web version of this article.)

the vortex is far enough from the patch (large $\delta\phi$) to allow for significant field-flow interaction, resulting in dominance of toroidal advection (Fig. 7). This effect produces a bipolar SV with its negative structure (same sign as the field) upwind.

In case 2 (Fig. 8) the vortex and flux patch are aligned, so no SV is generated by toroidal advection, and magnetic field stretching by fluid downwelling is responsible for most of the SV. Since the downwelling is centered at the peak field intensity, a very localized SV structure appears at the same location. The downwelling concentrates (negative) flux to produce negative SV, i.e. flux intensification. Note that when the patch width exceeds the vortex width ($\sigma > H$, as is the case here) advection by poloidal flow is rather weak because the stronger poloidal flow is confined to a region where ∇B_r is small. However, when $H > \sigma$ a ring of positive SV due to advection by poloidal flow is formed around the negative stretching SV structure.

Stronger relative poloidal flow (i.e. larger k) and an intermediate distance between the vortex and the flux patch give a combined advection/stretching SV (case 3, Fig. 9). Here the superposition of negative SV due to stretching and symmetric bipolar SV due to advection yields an asymmetric bipolar SV. The stronger negative part is found at the north due to northward advection of negative field by the eastern limb of the vortex. Because the downwelling is restricted to the inner part of the vortex, the stretching structure is closer to the vortex than to the magnetic flux patch.

In case 4, the same field-flow configuration is kept as in case 3, but in addition the effect of magnetic field diffusion is added (Fig. 10). Diffusion weakens the field, inducing a positive SV contribution at the same location as the flux patch. The asymmetric bipolar SV structure, which in case 3 was stronger at the negative (northern) side due to the downwelling, is here stronger at the positive (southern) side due to the action of diffusion.

The dependence of the forward models on the free parameters is further illustrated in Fig. 11. For small offset between the patch and the vortex $\delta\phi \sim 0^\circ$, stretching dominates the SV. Increasing $\delta\phi$ gives rise to advective SV, which exceeds stretching effects at small k. At large $\delta\phi$ the interaction between the field and the flow diminishes (Fig. 11 left). For a case with no offset, stronger poloidal flows yield stronger SV due to stretching, but the increase in SV is saturated at large k due the opposing effects of advection by poloidal flow (Fig. 11 middle). Finally, for small effective magnetic diffusivity $\lambda^* < 140$ induction effects dominate the SV. In this relatively large k case the peak SV is provided by stretching, with diffusion acting to reduce it. For $\lambda^* > 140$ diffusion dominates the SV.

3.3. Geomagnetic secular variation in a satellite field model

Before attempting to interpret the SV patterns in the stacked images (Figs. 2–5) using the idealized cases (Figs. 7–10), it is worth-while examining the patches and their SV in a recent high-quality geomagnetic field model constructed from satellite data. Although this field model spans a short period and stacking is probably not very meaningful, its much better spatial resolution deserves examination. In Fig. 12, the radial field and its SV centered below the North America, Siberia and Southern Indian Ocean patches are shown based on the *CHAOS-4* satellite-based geomagnetic field model of Olsen et al. (2010). The flux patch below the Southern Pacific Ocean has already decreased its intensity at the end of the period covered by *gufm1* (Amit et al., 2011), and the field map from *CHAOS-4* suggests that this trend is continuing. I therefore avoid interpreting the SV associated with this flux patch, which may not be classified as intense at present.

The geomagnetic flux patch below North America (Fig. 12 top left) shows a bipolar structure suggestive of northwest drift direction, as in the corresponding stacked image (Fig. 2 bottom). However, unlike the stacked image, the zero SV contour in the 2005 snapshot does not coincide with the peak field. Overall, the qualitative agreement is suggestive of a continuous kinematic behavior. Below Siberia (Fig. 12 top right) an asymmetric bipolar SV structure may be identified. Finally, the radial field and its SV below the Southern Indian Ocean patch (Fig. 12 bottom) show an overall

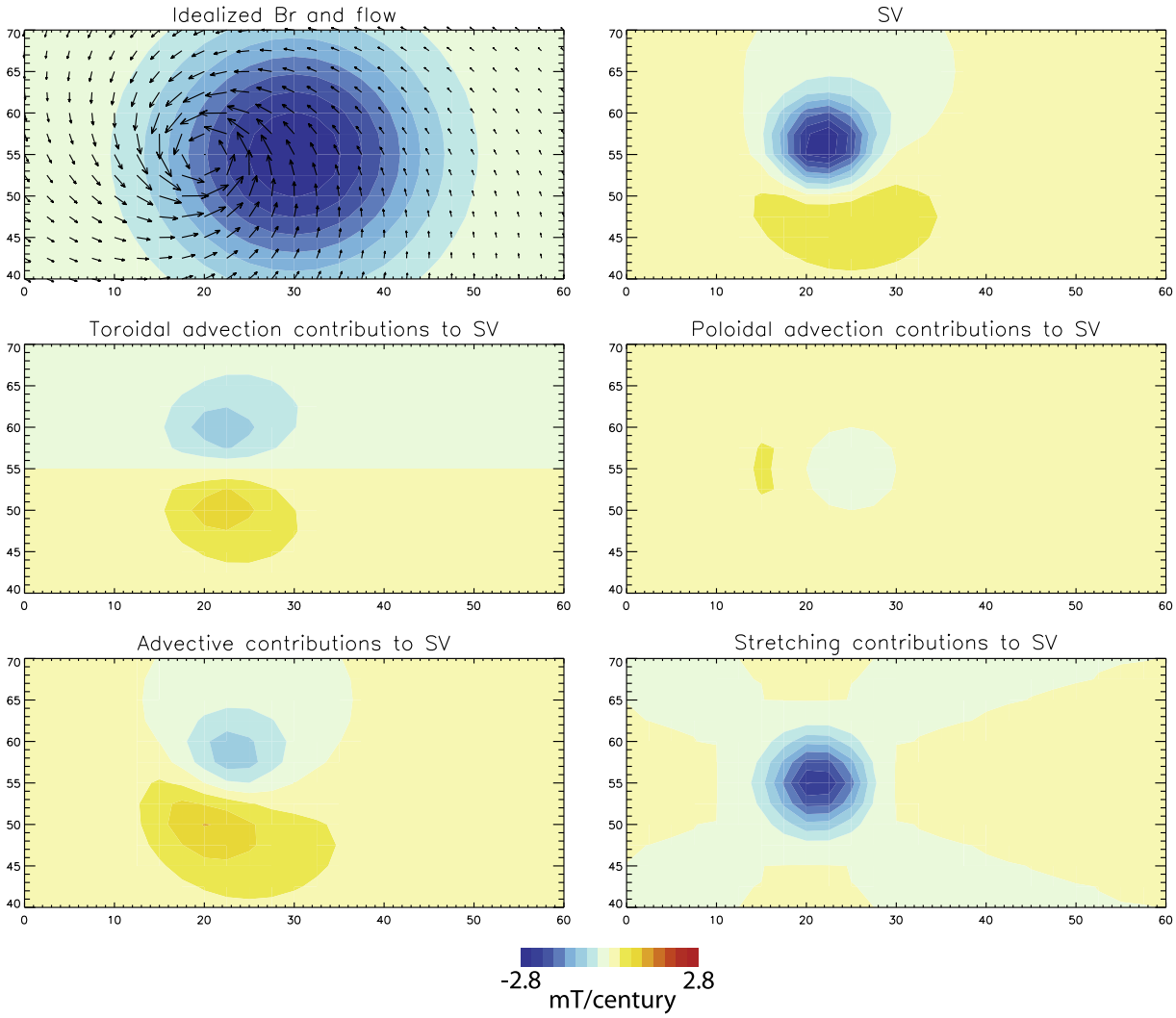

Fig. 9. As in Fig. 7 for idealized case 3: combined advection/stretching.

same-sign (positive) SV suggestive of field intensification, just as in the corresponding stacked image (Fig. 5).

4. Discussion

The idealized forward models rely on extremely simple and highly uncertain assumptions, so caution is required when inferring their patterns to interpret geomagnetic SV models. Nevertheless, the assumptions are motivated by some observations, numerical simulations and theoretical considerations. The Gaussian model for a flux patch is in adequate agreement with the stacked geomagnetic radial field at these regions (Fig. 6). The Rankine vortex is commonly used in atmospheric sciences and oceanography for describing large-scale systems (Ghil and Solan, 1973; Ide and Ghil, 1997; Brown et al., 2005; Harvey and Ambaum, 2011). The helical flow assumption that couples the toroidal and poloidal flows has been observed in numerical dynamos (Olson et al., 2002; Amit et al., 2007) and may be especially applicable for high-latitudes where axial convective columns impinge the CMB (Amit et al., 2010). When downward projected through an axial convective column, helical flow yields significant helicity (Olson et al., 1999), which is an essential ingredient for dynamo action (Moffatt, 1978).

Bearing in mind these oversimplified assumptions, the idealized forward SV models may be viewed as a zeroth order qualitative demonstration of simple SV patterns that may be expected from various kinematic scenarios at regions of intense magnetic flux patches. Advection of intense magnetic flux patch by a jet yields a symmetric bipolar SV pattern (Fig. 7). If the flow is aligned with the field, the stretching effect gives a monopolar SV at the same location and of the same sign as the flux patch (Fig. 8). Combined advection/stretching results in an asymmetric bipolar SV with the stronger pole being of the same sign as the flux patch (Fig. 9). Magnetic flux may be destroyed by radial diffusion - in that case the asymmetric bipolar SV is characterized by a stronger pole being of the opposite sign to the flux patch (Fig. 10).

Elements of some of these idealized SV patterns can be identified in the stacked geomagnetic SV images. The North America and Siberia patches exhibit symmetric bipolar patterns, indicating plain translation of the patches by advection, i.e. persistent drift (compare Figs. 2 bottom and 3 with Fig. 1). Note that in these stacked images the zero SV contour is well correlated with the peak field intensity, as expected from translational advective SV. The Southern Pacific Ocean patch also shows a bipolar pattern suggestive of advective effects, though it is less symmetric (Fig. 4). The stacked radial field and SV of the Southern Indian Ocean patch are both positive (Fig. 5), providing an indication of persistent down-

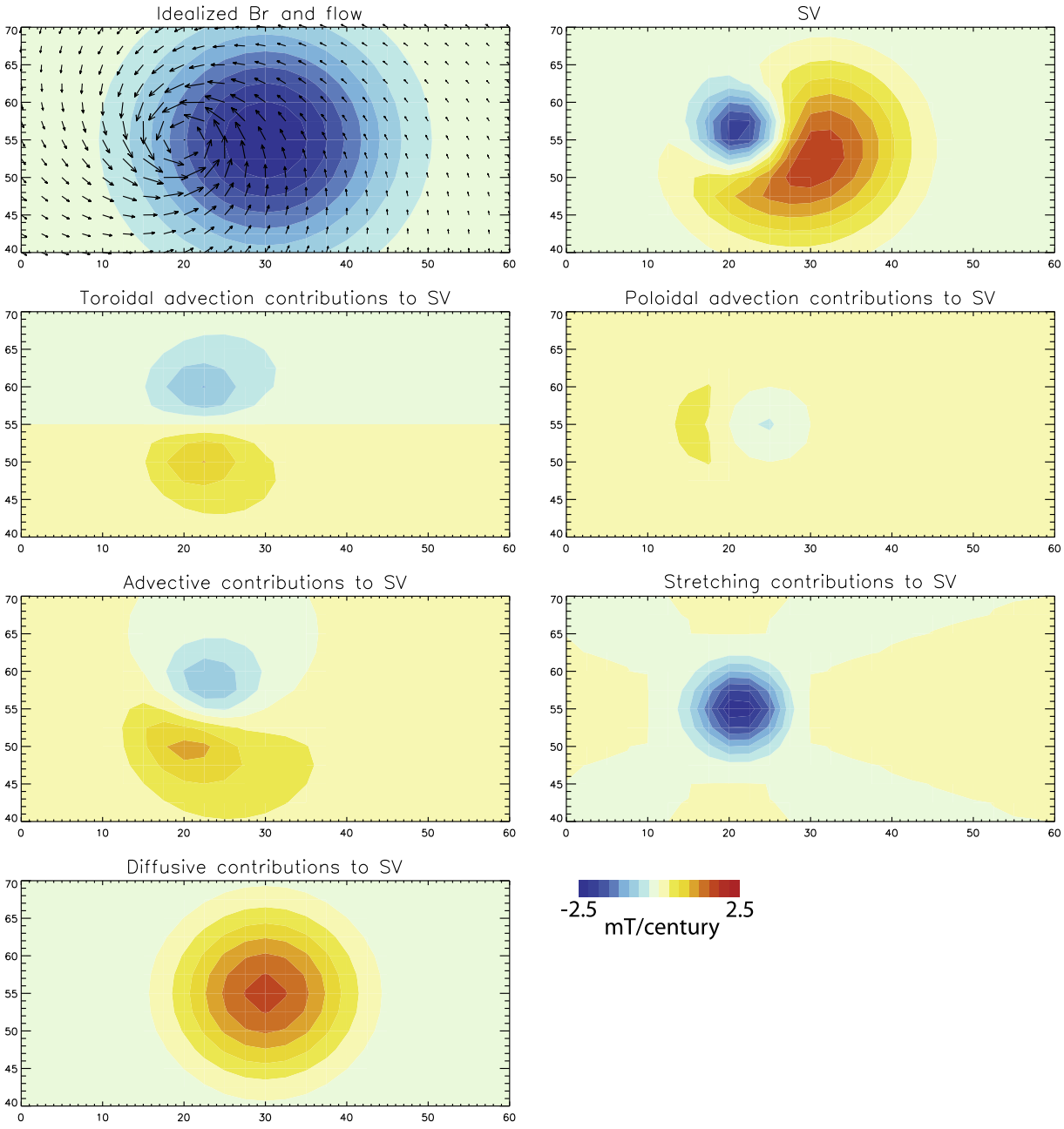

Fig. 10. As in Fig. 7 for idealized case 4: diffusion. Here an additional subplot of diffusive contributions to SV was added (bottom left).

welling activity that has been concentrating field lines and intensifying the radial field at this region.

The dependence of the forward models on the free parameters may be used to provide some rough bound estimates on these parameters. In the stacked SV images the peak values range $0.2-0.5$ (Figs. 2–5). Based on Fig. 11, this corresponds to $\delta\phi \sim 25^\circ - 35^\circ$ and $k \sim 0.05-0.1$, which may be considered as upper/lower bounds of these parameters respectively. In the regime where diffusion dominates the peak SV values are much larger than the values of the stacked images, suggesting that the time-dependence of the intense geomagnetic flux patches is not governed by magnetic diffusion.

Examination of the SV below the intense flux patches of the recent high quality geomagnetic field model *CHAOS-4* (Fig. 12) shows some continuation of the same trends identified in the stacked images of the historical field. Below North America a symmetric bipolar SV is still identified, with its axis pointing to the northwest, in agreement with the drift direction found by Amit et al. (2011) for this patch during the historical period. In this snapshot the zero SV contour is a bit shifted from the peak field intensity, demonstrating the rapid variations in the field-flow interactions in the outer core. The Southern Indian Ocean patch is once again well correlated with positive SV, providing evidence for present-day downwelling activity at that region. In contrast, the modern snapshot below Siberia is rather different from the stacked images at that region.

The clear advective SV signature below North America indicates that the intense flux patches are mobile, in contrast to the proposed scenario of complete locking to mantle heterogeneity (Gubbins et al., 2007). This mobility is in agreement with the findings of Amit et al. (2011) based on tracking in time the positions of the centers of patches. Diffusive SV signatures have not been detected.

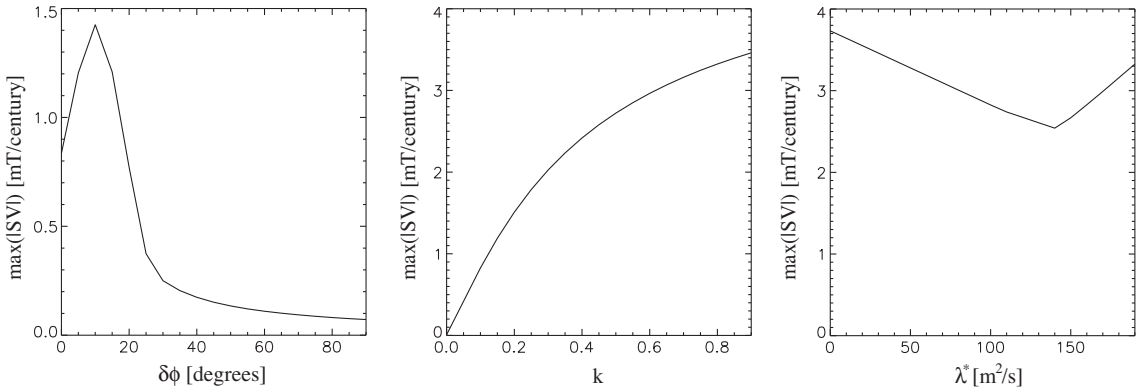

Fig. 11. Dependence of the maximum of the idealized SV on the free parameters. Left: Maximum absolute SV vs. $\delta\phi$ with $k = 0.1$ and $\lambda^* = 0$; Middle: Maximum absolute SV vs. k with $\delta\phi = 0^\circ$ and $\lambda^* = 0$; Right: Maximum absolute SV vs. λ^* with $\delta\phi = 10^\circ$ and $k = 0.5$.

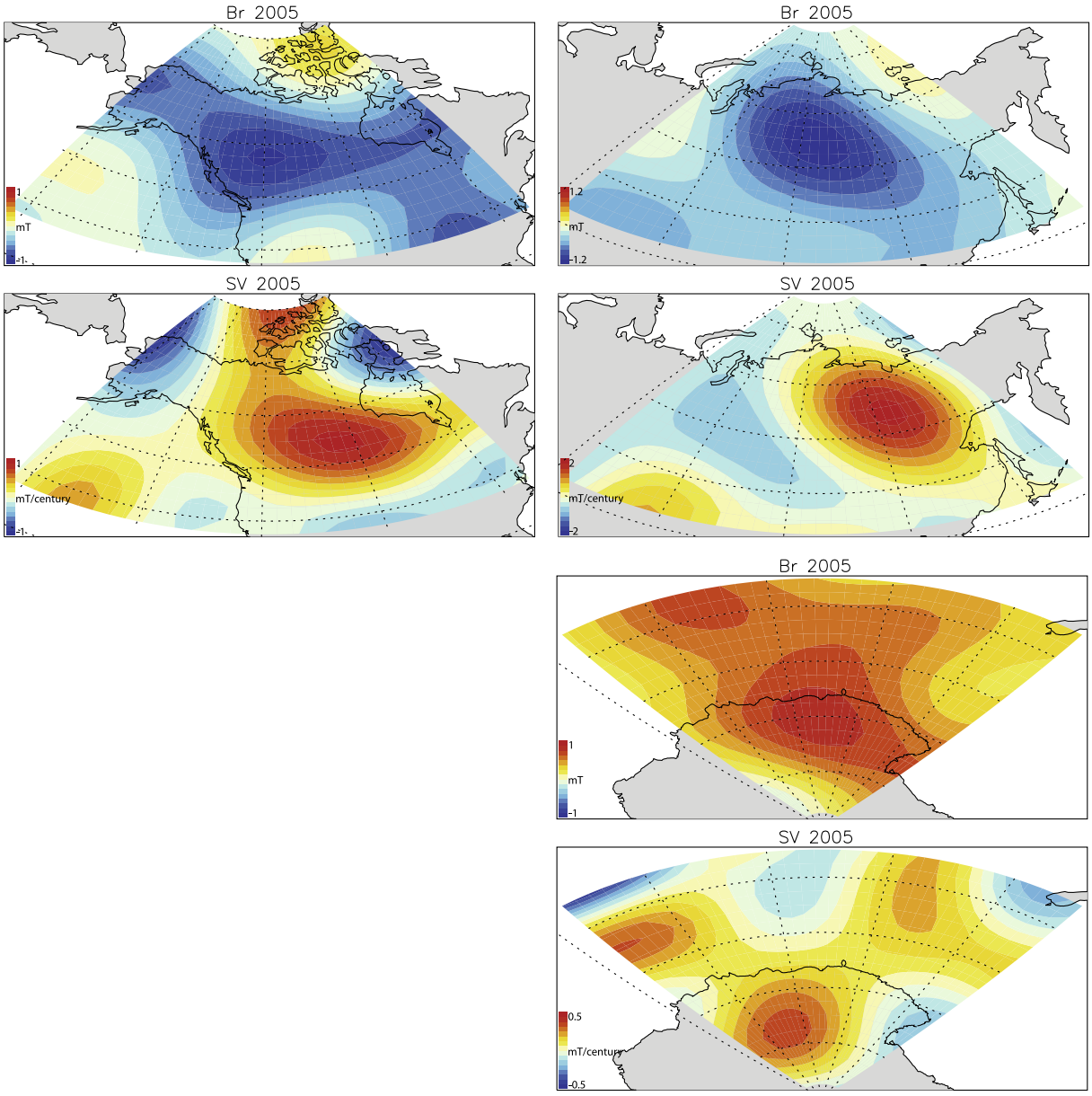

Fig. 12. Radial field and SV at 2005 based on the geomagnetic field model *CHAOS-4* of Olsen et al. (2010) centered below the North America flux patch (top left), the Siberia patch (top right) and the Southern Indian Ocean patch (bottom).

Diffusion is likely to play an important role at regions where reversed flux emerges (e.g. Bloxham, 1986). At high-latitudes diffusion may act as a saturation mechanism for the intense flux patches. The lack of diffusive signature in the stacked SV suggests that the patches are not yet fully saturated. An exception is the patch below Southern Pacific Ocean which is currently much weaker than the other three patches.

The main implication of the results obtained in this paper concerns the likelihood of stable stratification at the top of the core. The persistent positive stacked SV signature near the intense geomagnetic flux patch below the Southern Indian Ocean is suggestive of the existence of downwelling activity at this region throughout the historical period. The SV from the recent satellite-based *CHAOS-4* field model further indicates that field concentration by downwelling below the Southern Indian Ocean continues nowadays.

Upwelling/downwelling activity below the Indian Ocean was detected by core flow inversion studies that employed various physical assumptions (Gire and LeMouël, 1990; Amit and Olson, 2006; Amit and Pais, 2013). Olson and Amit (2006) combined core field and flow models to map meridional advection contributions to axial dipole change. They found the largest contribution below the Indian Ocean where geomagnetic flux is advected equatorward. At low-latitudes below the Indian Ocean, flux patches are concentrated and later drift westward (Jackson et al., 2000; Finlay and Jackson, 2003). In general, the fit to the geomagnetic SV by inverted core flows is greatly improved when poloidal flow is permitted (Beggan and Whaler, 2008). Regional SV analyses inferred core upwelling at the north polar region where a reversed flux patch has been emerging (Olson and Aurnou, 1999; Chulliat et al., 2010). These global and regional scale SV inferences lead to the same conclusion as the results reported in this study - the geomagnetic SV morphology, in particular at some specific CMB regions, may reflect the kinematics of magnetic field stretching by fluid upwelling/downwelling.

It is important to emphasize that the results of this study merely point to a simple kinematic scenario based on some inferrences from theory and numerical dynamos concerning the presence of local downwelling structures that maintain high-latitude intense magnetic flux patches. However, the non-uniqueness associated with inferring global core flow from geomagnetic SV also applies in the regional scale, so the existence of a poloidal flow cannot be proven. In fact, it is probable that the regional SV below the Indian Ocean could also be explained by a purely toroidal flow. It therefore remains an open question whether whole core convection can be invoked from the geomagnetic SV.

Appendix A. Rotational transformation about a center of a patch

Any rotational transformation to a given spatial function on a surface of a sphere produces two types of deformations: Translational and rotational. If the axis of a center of a structure is perpendicular to the axis of rotation, the structure will be translated; If the axis of a center of a structure coincides with the axis of rotation, the structure will be rotated about its axis. In order to rotate about a center of a magnetic flux patch, three steps are taken: Translation to the north geographic pole, rotation about the pole, and translation back to the center of the patch.

For convenience, the Cartesian x-axis is defined at the longitude of the center of the patch. The translations are therefore performed by rotational transformations about the Cartesian y-axis, and the rotation is performed about the Cartesian z-axis that points to the north geographic pole. The translation from the center of the patch at co-latitude θ_0 to the north pole is described by the following matrix:

$$R_{yn} = \begin{pmatrix} \cos(-\theta_0) & 0 & -\sin(-\theta_0) \\ 0 & 1 & 0 \\ \sin(-\theta_0) & 0 & \cos(-\theta_0) \end{pmatrix} \tag{A-1}$$

The rotational transformation is determined by the vector connecting two successive patches. For small translations, a local Cartesian coordinate system allows approximating the rotation angle by

$$\omega = atan\left(\frac{\Delta\theta}{\Delta\phi \sin\theta_0}\right) \tag{A-2}$$

where $\Delta\theta = \theta(t_i) - \theta(t_{i-1})$ and $\Delta\phi = \phi(t_i) - \phi(t_{i-1})$. The rotational transformation is then performed about the north geographic pole:

$$R_w = \begin{pmatrix} \cos\omega & -\sin\omega & 0 \\ \sin\omega & \cos\omega & 0 \\ 0 & 0 & 1 \end{pmatrix} \tag{A-3}$$

Finally, the translation that returns the patch to its original center at co-latitude θ_0 is

$$R_{ys} = \begin{pmatrix} \cos\theta_0 & 0 & -\sin\theta_0 \\ 0 & 1 & 0 \\ \sin\theta_0 & 0 & \cos\theta_0 \end{pmatrix} \tag{A-4}$$

The three rotational transformation matrices can be gathered into one matrix describing the rotational transformation about the center of a patch:

$$R = R_{yn} \cdot R_w \cdot R_{ys} = \begin{pmatrix} \cos^2\theta_0 \cos\omega + \sin^2\theta_0 & -\cos\theta_0 \sin\omega & \cos\theta_0 \sin\theta_0(1-\cos\omega) \\ \cos\theta_0 \sin\omega & \cos\omega & -\sin\theta_0 \sin\omega \\ \cos\theta_0 \sin\theta_0(1-\cos\omega) & \sin\theta_0 \sin\omega & \sin^2\theta_0 \cos\omega + \cos^2\theta_0 \end{pmatrix} \tag{A-5}$$

To map a point (ϕ, θ) in the original grid around the center of a patch to a point (ϕ', θ') in the new grid rotated by an angle ω about the center of the patch, the following steps are taken. First the spherical coordinates (ϕ, θ) are transformed to Cartesian coordinates (x, y, z). Next the rotational transformations are applied to obtain the rotated point in Cartesian coordinates (x', y', z'):

Acknowledgments

This study was supported by the Centre National d'Études Spatiales (CNES). I am grateful to Gauthier Hulot and Chris Davies for constructive comments that significantly improved this paper. I thank Benoit Langlais and Eric Beucler for insightful discussions.

$$\begin{pmatrix} x' \\ y' \\ z' \end{pmatrix} = R \cdot \begin{pmatrix} x \\ y \\ z \end{pmatrix} \tag{A-6}$$

Finally, the rotated point is transformed from Cartesian (x', y', z') to spherical coordinates (ϕ', θ').

References

Amit, H., Aubert, J., Hulot, G., 2010. Stationary, oscillating or drifting mantle-driven geomagnetic flux patches? J. Geophys. Res. B07108. http://dx.doi.org/10.1029/2009JB006542.

Amit, H., Christensen, U., 2008. Accounting for magnetic diffusion in core flow inversions from geomagnetic secular variation. Geophys. J. Int. 175, 913–924.

Amit, H., Korte, M., Aubert, J., Constable, C., Hulot, G., 2011. The time-dependence of intense archeomagnetic flux patches. J. Geophys. Res. 116, B12106. http://dx.doi.org/10.1029/2011JB008538.

Amit, H., Olson, P., 2004. Helical core flow from geomagnetic secular variation. Phys. Earth Planet. Inter. 147, 1–25.

Amit, H., Olson, P., 2006. Time-average and time-dependent parts of core flow. Phys. Earth Planet. Inter. 155, 120–139.

Amit, H., Olson, P., Christensen, U., 2007. Tests of core flow imaging methods with numerical dynamos. Geophys. J. Int. 168, 27–39.

Amit, H., Pais, M.A., 2013. Differences between tangential geostrophy and columnar flow. Geophys. J. Int. 194, 145–157.

Beggan, C., Whaler, K., 2008. Core flow modelling assumptions. Phys. Earth Planet. Inter. 167, 217–222.

Bloxham, J., 1986. The expulsion of magnetic flux from the Earth's core. Geophys. J.R. Astr. Soc. 87, 669–678.

Bloxham, J., 1989. Simple models of fluid flow at the core surface derived from geomagnetic field models. Geophys. J. Int. 99, 173–182.

Bloxham, J., 1992. The steady part of the secular variation of the Earth's magnetic field. J. Geophys. Res. 97, 19565–19579.

Bloxham, J., 2002. Time-independent and time-dependent behaviour of high-latitude flux bundles at the core–mantle boundary. Geophys. Res. Lett. 29. http://dx.doi.org/10.1029/2001gl014543.

Bloxham, J., Jackson, A., 1991. Fluid flow near the surface of the Earth's outer core. Rev. Geophys. 29, 97–120.

Brown, R.A., Flikinger, B.A., Forren, E., Schultz, D.M., Sirmans, D., Spencer, P.L., Wood, V.T., Ziegler, C.L., 2005. Improved detection of severe storms using experimental fine-resolution wrs-88d measurements. Weather Forecasting 20, 3–14.

Christensen, U., Aubert, J., Hulot, G., 2010. Conditions for Earth-like geodynamo models. Earth Planet. Sci. Lett. 296, 487–496.

Christensen, U., Olson, P., Glatzmaier, G., 1998. A dynamo model interpretation of geomagnetic field structures. Geophys. Res. Lett. 25, 1565–1568.

Chulliat, A., Hulot, G., Newitt, L.R., 2010. Magnetic flux expulsion from the core as a possible cause of the unusually large acceleration of the North magnetic pole during the 1990s. J. Geophys. Res. 115, B07101. http://dx.doi.org/10.1029/2009JB007143.

Chulliat, A., Olsen, N., 2010. Observation of magnetic diffusion in the Earth's outer core from Magsat, Orsted and CHAMP data. J. Geophys. Res. 115. http://dx.doi.org/10.1029/2009JB006994.

Finlay, C., Jackson, A., 2003. Equatorially dominated magnetic field change at the surface of Earth's core. Science 300, 2084–2086.

Finlay, C.C., Amit, H., 2011. On flow magnitude and field-flow alignment at Earth's core surface. Geophys. J. Int. 186, 175–192.

Ghil, M., Solan, A., 1973. Heat transfer through a Rankine vortex. J. Heat Transfer 33, 137–139.

Gire, C., LeMouël, J.-L., 1990. Tangentially-geostrophic flow at teh core–mantle boundary compatible with the observed geomagnetic secular variation: the large-scale component of the flow. Phys. Earth Planet. Inter. 59, 259–287.

Gubbins, D., 1982. Finding core motions from magnetic observations. Philos. Trans. R. Soc. London Ser., A. 306, 249–256.

Gubbins, D., 2003. Thermal core–mantle interactions: theory and observations. In: Dehant, V., Creager, K., Karato, S., Zatman, S. (Eds.), Earth's Core: Dynamics, Structure and Rotation. AGU Geodynamics Series American Geophysical Union.

Gubbins, D., Davies, C.J., 2013. The stratified layer at the core–mantle boundary caused by barodiffusion of oxygen, sulphur and silicon. Phys. Earth Planet. Inter. 215, 21–28.

Gubbins, D., Willis, P., Sreenivasan, B., 2007. Correlation of Earth's magnetic field with lower mantle thermal and seismic structure. Phys. Earth Planet. Inter. 162, 256–260.

Harvey, B.J., Ambaum, M.H.P., 2011. Perturbed Rankine vortices in surface quasi-geostrophic dynamics. Geophys. Astrophys. Fluid Dyn. 105, 377–391.

Helffrich, G., Kaneshima, S., 2010. Outer-core compositional stratification from observed core wave speed profiles. Nature 468, 807–810.

Holme, R., 2007. Large-scale flow in the core. In: Olson, P. (Ed.), Treatise on Geophysics, vol. 8. Elsevier Science.

Holme, R., Olsen, N., 2006. Core surface flow modelling from high-resolution secular variation. Geophys. J. Int. 166, 518–528.

Hulot, G., Eymin, C., Langlais, B., Mandea, M., Olsen, N., 2002. Small-scale structure of the geodynamo inferred from oersted and magsat satellite data. Nature 416, 620–623.

Ide, K., Ghil, M., 1997. Extended Kalman filtering for vortex systems. Part II: rankine vortices and observing-system design. Dyn. Atmos. Oceans 27, 333–350.

Jackson, A., Jonkers, A., Walker, M., 2000. Four centuries of geomagnetic secular variation from historical records. Philos. Trans. R. Soc. London A358, 957–990.

Kelly, P., Gubbins, D., 1997. The geomagnetic field over the past 5 million years. Geophys. J. Int. 128, 315–330.

Korte, M., Donadini, F., Constable, C., 2009. The geomagnetic field for 0–3 ka: 2. a new series of time-varying global models. J. Geophys. Res. 10, Q06008. http://dx.doi.org/10.1029/2008GC002297.

Lay, T., Hernlund, J., Buffett, B.A., 2008. Core–mantle boundary heat flow. Nature 1, 25–32.

Lay, T., Wallace, T.C., 1995. Modern global seismology. Academic Press, International Geophysics Series, vol. 58, San Diego, CA, USA.

Moffatt, H., 1978. Magnetic Field Generation in Electrically Conducting Fluids. Cambridge University Press, Cambridge, U.K..

Olsen, N., Luehr, H., Sabaka, T.J., Michaelis, I., Rauberg, J., Tffner-Clausen, L., 2010. CHAOS-4 - A high-resolution geomagnetic field model derived from low-altitude CHAMP data. In AGU Fall Meeting, Abstract GP21A–0992.

Olsen, N., Mandea, M., 2008. Rapidly changing flows in the Earth's core. Nat. Geosci. 1, 390–394.

Olson, P., 2007. Gravitational dynamos and the low frequency geomagnetic secular variation. Proc. Natl. Acad. Sci. 104, 20159–20166.

Olson, P., Amit, H., 2006. Changes in earth's dipole. Naturwissenschaften 93, 519–542.

Olson, P., Aurnou, J., 1999. A polar vortex in the Earth's core. Nature 402, 170–173.

Olson, P., Christensen, U., 2002. The time averaged magnetic field in numerical dynamos with nonuniform boundary heat flow. Geophys. J. Int. 151, 809–823.

Olson, P., Christensen, U., Glatzmaier, G., 1999. Numerical modeling of the geodynamo: mechanisms of field generation and equilibration. J. Geophys. Res. 104, 10383–110404.

Olson, P., Sumita, I., Aurnou, J., 2002. Diffusive magnetic images of upwelling patterns in the core. J. Geophys. Res. 107. http://dx.doi.org/10.1029/2001jb000384.

Pozzo, M., Davies, C., Gubbins, D., Alfè, D., 2012. Thermal and electrical conductivity of iron at Earth's core conditions. Nature 485, 355–358.

Rankine, W.J.M., 1858. Manual of Applied Mechanics. C. Griffen Co., London, UK.

Rau, S., Christensen, U., Jackson, A., Wicht, J., 2000. Core flow inversion tested with numerical dynamo models. Geophys. J. Int. 141, 485–497.

Roberts, P., Scott, S., 1965. On analysis of the secular variation, 1, a hydromagnetic constraint: Theory. J. Geomagn. Geoelec. 17, 137–151.

Shearer, P., 1991. Imaging global body wave phases by stacking long-period seismograms. J. Geophys. Res. 96, 20353–20364.

Valet, J.P., Fournier, A., Courtillot, V., Herrero-Bervera, E., 2012. Dynamical similarity of geomagnetic field reversals. Nature 490, 89–93.

Vlcek, V., de Koker, N., Steinle-Neumann, G., 2012. Electrical and thermal conductivity of Al liquid at high pressures and temperatures from ab initio computations. Phys. Rev. B 85. http://dx.doi.org/10.1103/PhysRevB.85.184201.

Whaler, K., 1980. Does the whole of Earth's core convect? Nature 287, 528–530.

Whaler, K., 1986. Geomagnetic evidence for fluid upwelling at the core–mantle boundary. Geophys. J. R. Astron. Soc. 86, 563–588.

Whaler, K., Holme, R., 2007. Consistency between the flow at the top of the core and the frozen-flux approximation. Earth Planets Space 59, 1219–1229.